Oxygen Transport Ceramic Membranes

Quarterly Report

July 2003 – September 2003

Principal Authors:

Prof. S. Bandopadhyay

Dr. N. Nagabhushana

Issued: November 2003

School of Mineral Engineering,
University of Alaska Fairbanks
Fairbanks, AK 99775

Contributing sub contractors:

1. **Prof. Thomas W. Eagar, Dr. Harold R Larson, Mr. Raymundo Arroyave**;
    Massachusetts Institute of Technology, Department of Materials Science and Engineering,
    Cambridge, Massachusetts 02139
2. **X.-D Zhou, Y.-W. Shin, and H. U. Anderson**, Materials Research Center, University of
    Missouri-Rolla, Rolla, MO 65401
3. **Prof. Nigel Browning;** Department of Chemical Engineering and Materials Science,
    University of California-Davis, One Shields Ave, Davis, CA 95616
4. **Prof. Alan Jacobson and Prof. C.A. Mims;** University of Houston/University of Toronto

DISCLAIMER

This report was prepared as an account of work sponsored by an agency of the United States Government. Neither the United States Government nor any agency thereof, nor any of their employees, makes any warranty, express or implied, or assumes any legal liability or responsibility for the accuracy, completeness, or usefulness of any information, apparatus, product, or process disclosed, or represents that its use would not infringe privately owned rights. Reference herein to any specific commercial product, process, or service by trade name, trademark, manufacturer, or otherwise does not necessarily constitute or imply its endorsement, recommendation, or favoring by the United States Government or any agency thereof. The views and opinions of authors expressed herein do not necessarily state or reflect those of the United States Government or any agency thereof

ABSTRACT

The present quarterly report describes some of the initial studies on newer compositions and also includes newer approaches to address various materials issues such as in metal-ceramic sealing. The current quarter's research has also focused on developing a comprehensive reliability model for predicting the structural behavior of the membranes in realistic conditions. In parallel to industry provided compositions, models membranes have been evaluated in varying environment. Of importance is the behavior of flaws and generation of new flaws aiding in fracture. Fracture mechanics parameters such as crack tip stresses are generated to characterize the influence of environment. Room temperature slow crack growth studies have also been initiated in industry provided compositions. The electrical conductivity and defect chemistry of an A site deficient compound ($La_{0.55}Sr_{0.35}FeO_3$) was studied. A higher conductivity was observed for $La_{0.55}Sr_{0.35}FeO_3$ than that of $La_{0.60}Sr_{0.40}FeO_3$ and $La_{0.80}Sr_{0.20}FeO_3$. Defect chemistry analysis showed that it was primarily contributed by a higher carrier concentration in $La_{0.55}Sr_{0.35}FeO_3$. Moreover, the ability for oxygen vacancy generation is much higher in $La_{0.55}Sr_{0.35}FeO_3$ as well, which indicates a lower bonding strength between Fe-O and a possible higher catalytic activity for $La_{0.55}Sr_{0.35}FeO_3$. The program continued to investigate the thermodynamic properties (stability and phase separation behaviour) and total conductivity of prototype membrane materials. The data are needed together with the kinetic information to develop a complete model for the membrane transport. Previous report listed initial measurements on a sample of $La_{0.2}Sr_{0.8}Fe_{0.55}Ti_{0.45}O_{3-x}$ prepared in-house by Praxair. Subsequently, a second sample of powder from a larger batch of sample were characterized and compared with the results from the previous batch.

TABLE OF CONTENTS

LIST OF GRAPHICAL MATERIALS

INTRODUCTION

Conversion of natural gas to liquid fuels and chemicals is a major goal for the Nation as it enters the 21st Century. Technically robust and economically viable processes are needed to capture the value of the vast reserves of natural gas on Alaska's North Slope, and wean the Nation from dependence on foreign petroleum sources. Technologies that are emerging to fulfill this need are all based syngas as an intermediate. Syngas (a mixture of hydrogen and carbon monoxide) is a fundamental building block from which chemicals and fuels can be derived. Lower cost syngas translates directly into more cost-competitive fuels and chemicals.

The currently practiced commercial technology for making syngas is either steam methane reforming (SMR) or a two-step process involving cryogenic oxygen separation followed by natural gas partial oxidation (POX). These high-energy, capital-intensive processes do not always produce syngas at a cost that makes its derivatives competitive with current petroleum-based fuels and chemicals.

In the mid 80's BP invented a radically new technology concept that will have a major economic and energy efficiency impact on the conversion of natural gas to liquid fuels, hydrogen, and chemicals.[1] This technology, called Electropox, integrates oxygen separation with the oxidation and steam reforming of natural gas into a single process to produce syngas with an economic advantage of 30 to 50 percent over conventional technologies.[2]

The Electropox process uses novel and proprietary solid metal oxide ceramic oxygen transport membranes [OTMs], which selectively conduct both oxide ions and electrons through their lattice structure at elevated temperatures.[3] Under the influence of an oxygen partial pressure gradient, oxygen ions move through the dense, nonporous membrane lattice at high rates with 100 percent selectivity. Transported oxygen reacts with natural gas on the fuel side of the ceramic membrane in the presence of a catalyst to produce syngas.

In 1997 BP entered into an OTM Alliance with Praxair, Amoco, Statoil and Sasol to advance the Electropox technology in an industrially sponsored development program. These five companies have

[1]Mazanec, T. J.; Cable, T. L.; Frye, J. G., Jr.; US 4,793,904, 27 Dec **1988**, assigned to The Standard Oil Company (now BP America), Mazanec, T. J.; Cable, T. L.; US 4,802,958, 7 Feb **1989**, assigned to the Standard Oil Co. (now BP America), Cable, T. L.; Mazanec, T. J.; Frye, J. G., Jr.; European Patent Application 0399833, 24 May **1990**, published 28 November **1990.**

[2]Bredesen, R.; Sogge, J.; "A Technical and Economic Assessment of Membrane Reactors for Hydrogen and Syngas Production" presented at Seminar on the Ecol. Applic. of Innovative Membrane Technology in the Chemical Industry", Cetraro, Calabria, Italy, 1-4 May **1996**.

[3]Mazanec, T.J., *Interface*, **1996**; Mazanec, T.J., *Solid State Ionics*, 70/71, **1994** 11-19; "Electropox: BP's Novel Oxidation Technology", T.J. Mazanec, pp 212-225, in "The Role of Oxygen in Improving Chemical Processes", M. Fetizon and W.J. Thomas, eds, Royal Society of Chemistry, London, **1993**; "Electropox: BP's Novel Oxidation Technology", T.J. Mazanec, pp 85-96, in "The Activation of Dioxygen and Homogeneous Catalytic Oxidation", D.H.R. Barton, A. E. Martell, D.T. Sawyer, eds, Plenum Press, New York, **1993**; "Electrocatalytic Cells for Chemical Reaction", T.J. Mazanec, T.L. Cable, J.G. Frye, Jr.; Prep Petrol Div ACS, San Fran, **1992** *37*, 135-146; T.J. Mazanec, T.L. Cable, J.G. Frye, Jr.; *Solid State Ionics*, **1992**, 53-56, 111-118.

been joined by Phillips Petroleum and now are carrying out a multi-year $40+ million program to develop and commercialize the technology. The program targets materials, manufacturing and engineering development issues and culminates in the operation of semi-works and demonstration scale prototype units.

The Electropox process represents a truly revolutionary technology for conversion of natural gas to synthesis gas not only because it combines the three separate unit operations of oxygen separation, methane oxidation and methane steam reforming into a single step, but also because it employs a chemically active ceramic material in a fundamentally new way. On numerous fronts the commercialization of Electropox demands solutions to problems that have never before been accomplished. Basic problems in materials and catalysts, membrane fabrication, model development, and reactor engineering all need solutions to achieve commercial success.

Six important issues have been selected as needing understanding on a fundamental level at which the applied Alliance program cannot achieve the breadth and depth of understanding needed for rapid advancement. These issues include:

1. Oxygen diffusion kinetics (University of Houston);
2. Grain structure and atomic segregation (University of Illinois - Chicago);
3. Phase stability and stress development (University of Missouri - Rolla);
4. Mechanical property evaluation in thermal and chemical stress fields (University of Alaska Fairbanks); and,
5. Graded ceramic/metal seals (Massachusetts Institute of Technology).

Statement of Work

Task 1   Design, fabricate and evaluate ceramic to metal seals based on graded ceramic powder / metal braze joints.

Task 2   Determine materials mechanical properties under conditions of high temperatures and reactive atmospheres.

Task 3   Evaluate phase stability and thermal expansion of candidate perovskite membranes and develop techniques to support these materials on porous metal structures.

Task 4   Assess the microstructure of membrane materials to evaluate the effects of vacancy-impurity association, defect clusters, and vacancy-dopant association on the membrane performance and stability.

Task 5   Measure kinetics of oxygen uptake and transport in ceramic membrane materials under commercially relevant conditions using isotope labeling techniques.

EXECUTIVE SUMMARY

Research on the Oxygen Transport Membranes as listed as tasks 1-5 are being performed at the various universities under the stewardship of Praxair. The technical report presents the progress of the various tasks defined to understand the fundamental concepts and the performance of the ceramic membrane in realistic conditions.

Throughout the development of this project, it has been found that, contrary to what is the case in the majority of the ceramic/metal applications encountered in industry, perovskite substrates are easily wetted, even by relatively inactive liquid alloys. This is of great importance, since this allows, at least in principle, the use of liquid-based joining techniques for the creation of ceramic/metal seals that are necessary for the proper functioning of the Gas-to-Liquid reactor system. In order to understand the thermochemical interactions occurring at the zirconia/Ti interface, a model based on the kinetics described by the Cahn-Hilliard equation was developed. It as found that this model describe, to a great degree of accuracy, the reaction sequence that is expected to happen as Ti is put in contact with zirconia. With the proper thermodynamic data, it may be possible to describe the nature of the interactions between the perovskite-based ceramics and the Ni-based liquids using similar models to the one described in this report. Eventually, the models will allow the better design of the joining procedure necessary to create a reliable perovskite/metal seal.

The complexities in the structural property characterization $La_{0.2}Sr_{0.8}Fe_{0.8}Cr_{0.2}O_{3-x}$ membranes have been an increased focus of study. Developing a comprehensive model incorporating initiation and growth of flaws and their relation to degradation process has been the focus in addressing reliability issues in the membrane. To better understand the effects of flaw initiation and growth, parallel work was initiated in model membrane compositions such as LSF, LSC and LSCF. Indentation techniques were used to generate reproducible flaws and in addition, toughness were measured at elevated temperature in two different conditions: i) in Air and ii) in a cycle of heating in N_2 and slowly switching the gas to air. The membranes indicated changes in toughness values after exposure to the environment. In air, all the composition tested indicated a degradation of ~ 25-35 % in toughness values. Exposure to the cycle (N_2/Air) indicated mixed results. A gradual recovery was observed in LSFCO composition (1.06 MPa.m$^{0.5}$ as compared to 0.84 MPa.m$^{0.5}$ in air) while in LSC, LSCF 6428 and 8282 an increase in toughness over that of room temperature was observed. Initial attempts were also made to evaluate the crack tip parameters by measuring the crack opening displacements, $u(r)$, behind the crack tip and relating to the stress intensity for the linear-elastic median (strength degrading parameter) crack tip. The indentation cracks upon exposure to elevated temperature (1000ºC) and environment indicted a decrease in the surface residual stress. The reduction in LSFCO OTM was calculated to be compressive and ~ 7 MPa in air and ~ 60MPa in N_2/Air. This would have an important implication in evaluating strength/toughness and reliability at elevated temperatures. The flaw would not be as observed at room temperature and also the compressive stress may mean additional energy to be needed to initiate crack growth. Slow crack growth studies at room temperature, indicate small change in fracture strength. The fracture mechanisms need to be characterized and would be presented in the quarterly report.

Neutron diffraction and Mössbauer spectroscopy were used to characterize the perovskite type ferrites, in terms of the crystal structure, oxygen occupancy, magnetic moment, and Fe valence state. The electrical conductivity and defect chemistry of an A site deficient compound ($La_{0.55}Sr_{0.35}FeO_3$) was studied. A higher conductivity was observed for $La_{0.55}Sr_{0.35}FeO_3$ than that of $La_{0.60}Sr_{0.40}FeO_3$ and $La_{0.80}Sr_{0.20}FeO_3$. Defect chemistry analysis showed that it was primarily contributed by a higher carrier concentration in $La_{0.55}Sr_{0.35}FeO_3$. Moreover, the ability for oxygen vacancy generation is much higher in $La_{0.55}Sr_{0.35}FeO_3$ as well, which indicates a lower bonding strength between Fe-O and a possible higher catalytic activity for $La_{0.55}Sr_{0.35}FeO_3$. The maximum in

conductivity represents the temperature at which the oxygen vacancy concentration starts to influence the carrier concentration. It does not mean that the oxygen vacancy concentration is negligible at this temperature, but on the other hand, the influence of oxygen vacancy concentration on total carrier concentration is negligible below this temperature and the concentration of oxygen vacancies is so small that their contribution to transport processes becomes minimal. The oxygen activity dependence of the electrical conductivity of L55SF indicates that equilibrium is very easy to achieve (several hours) when oxygen partial pressure is higher than 10^{-2} atm. A much long equilibrium time is required for measuring stable conductivity value when P_{O2} is less than 10^{-3} atm (normally ~ couple of days). The conductivity leveled out for 1000 and 900°C, when the P_{O2} decreased below 10^{-4} atm. Similar behavior has been observed for other compounds in LSF series at relatively low temperature (< 900°C). This needs to be further investigated in other complex membranes.

Studies were continued to investigate the thermodynamic properties (stability and phase separation behavior) and total conductivity of prototype membrane materials. The data are needed together with the kinetic information to develop a complete model for the membrane transport. Previously initial measurements were reported on a sample of $La_{0.2}Sr_{0.8}Fe_{0.55}Ti_{0.45}O_{3-x}$ prepared in-house by Praxair. Subsequently, a second sample of powder from a larger batch of sample were characterized and compared with the previous batch. The results are similar for the two batches. The conductivity shows Arrhenius behavior at temperatures lower than about 300 °C. The activation energy increases with decreasing oxygen partial pressure as the contribution from ionic conductivity to the total conductivity increases. The maximum conductivity observed in $pO_2 = 1$ atm is ~10 S cm^{-1} and is significantly higher for batch #2. Above 300 °C, the conductivity falls as the oxygen stoichiometry increases and at higher oxygen pressures, the plateau observed in the conductivity for the batch #1 sample is not observed for batch #2. The SIMS result on LSCF shows that *O fraction varies with angle, indicating substantial heterogeneity in the sample. Approximately a factor of two was observed in the peak isotope fraction with angle. Some of this heterogeneity may have been induced by the water vapor treatment. The isotope fraction shows a hot spot in the upper part of the image which is close to a crack in the removed sample. This region was probably associated with a weak spot or incomplete crack in the sample. Other cracks in the removed sample do not show unusual isotope composition, indicating that they were induced largely by the thermal shock during cooling. The radial distribution at each angular region can be analyzed to obtain local surface and bulk mobilities. This work along with initial studies on LSCrF is in progress.

Task 1   **Development of Ceramic Membrane/Metal Joints**

Prof. Thomas W. Eagar, Dr Harold R Larson,
Mr Raymundo Arroyave and Ms Jocelyn L. Wiese

EXPERIMENTAL

No experimental work was conducted on this project during this reporting period due to failure to obtain continued funding beyond the initial twelve month period.

RESULTS AND DISCUSSION

This work has significantly enhanced our understanding of factors impacting the formation and stability of important ceramic to metal joints. This includes joints for systems important to the Gas to Liquids Fuels research. Thermal and kinetic phenomena at the interfaces were modeled. These models are in good agreement with experimentally determined phases observed in the experimental interface regions

Because of the high chemical affinity between O and Ti, a large oxygen chemical potential gradient is created across the C/M interface as soon as a ceramic oxide is put in contact with Ti. This gradient constitutes the driving force necessary to achieve bonding As oxygen vacancies are created, oxygen atoms diffuse towards the zirconia/Ti interface. As zirconia reacts with Ti, a sequence of titanium oxides is formed at the interface and the complex layering grows with time until chemical equilibrium is reached. According to experimental results the titanium reaction layer often found at zirconia/Ti interfaces is TiO_{1-x}. The nature of the first-forming titanium-oxygen compound at the *C/M* interface is determined by the interfacial oxygen chemical potential, which can be fixed by additional chemical reactions occurring in the system.

It has been shown that it is possible to model the Ti/zirconia thermochemical interactions through the solution of the so-called Cahn-Hilliard equation,
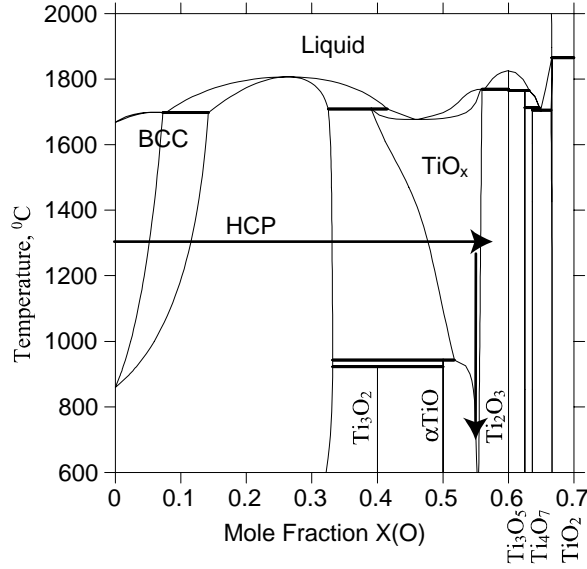
Figure 1 Ti-O Phase Diagram.

$$\frac{dc}{dt} = -\nabla \cdot M \cdot \nabla \left(\frac{\partial f}{\partial c} - 2k\nabla^2 c(x) \right)$$

$$= M \left(\nabla^2 \left(\frac{\partial f}{\partial c} \right) - 2k\nabla^4 c(x) \right)$$

(1.1)

Through the numerical solution of, it has been possible to describe the evolution of zirconia/Ti interactions. From the results, the reaction sequence through which bcc-Ti is transformed into a Ti-oxide can be observed

CONCLUSIONS

A better model for the thermochemical interactions between zirconia layers and Ti thin films allows a better estimation of the processing times necessary to obtain a stable interface in perovskite/metal applications where zirconia-based diffusion barriers are used to decrease the interaction between the TLPB alloy and the substrate itself. Furthermore, the model develop in this work may eventually be applied to describe the detrimental liquid metal/perovskite interactions that prevent the creation of reliable perovskite/metal interfaces without the use of protective diffusion barriers.

TASK 2:   Determine material mechanical properties under conditions of high temperature and reactive atmosphere

Prof. Sukumar Bandopadhyay and Dr. Nagendra Nagabhushana
University of Alaska Fairbanks

EXPERIMENTAL PROCEDURE

Beams of composition as mentioned in the previous report were fabricated. The samples were characterized by XRD, optical microscopy and density measurements. The toughness of the materials was measured by indentation technique and the median and radial cracks were observed in a Scanning Electron microscope. The indents were exposed to air and N_2/Air at 1000ºC to evaluate the characteristics of the indent before application of load. Post exposure sample were also indented to measure for degradation in toughness values. OTM bar samples provided by Praxair were evaluated for strength at room temperature and under varying loading rates. Initial studies were alos begun on evaluating strength in N_2/air at 1000ºC.

RESULTS AND DISCUSSIONS:

The results of the indentation hardness and toughness studies on Lanthanum based perovskite compositions are tabulated in table 1. As noted earlier, $La_{0.2}Sr_{0.8}Fe_{0.8}Cr_{0.2}O_{3-\delta}$ composition provided by the OTM alliance is studied along with model $La_xSr_{1-x}Fe_{1-y}Co_yO_{3-\delta}$ compositions in which the B site is varied from fully Co to fully Fe cation occupation. Along with the Co/Fe ratio on the B site and the La/Sr ratio on the A site are also varied.

The measured indentation toughness of the model compositions corresponded to some of the values reported in literature. The previous report presented a graphical representation of the variation in hardness and toughness with indentation load. With increasing load, there was corresponding increase in crack length and in some instance (for ex: LSFCO) damage accumulation was observed around the indent.

Indentation toughness was also measured at elevated temperature in two different conditions: i) in Air and ii) in a cycle of heating in N_2 and slowly switching the gas to air. As shown in table 1, the test samples indicated changes in toughness values after exposure to the environment. In air, all the composition tested indicated a degradation of ~ 25-35 % in toughness values. Exposure to the cycle (N_2/Air) indicated mixed results. A gradual recovery was observed in LSFCO composition (1.06 MPa.m$^{0.5}$ as compared to 0.84 MPa.m$^{0.5}$ in air) while in LSC, LSCF 6428 and 8282 an increase in toughness over that of room temperature was observed.

Table 1: Indentation hardness and toughness of the composition in different environment

Composition	RT K_c, MPa.m$^{0.5}$	In Air, 1000 °C K_c, MPa.m$^{0.5}$	In N$_2$/Air 1000°C K_c, MPa.m$^{0.5}$
La$_{0.2}$Sr$_{0.8}$Cr$_{0.2}$Fe$_{0.8}$O$_{3-\delta}$ (LSFCO)	1.2 (± 0.11)	0.84 (± 0.08)	1.06 (± 0.21)
La$_{0.6}$Sr$_{0.4}$FeO$_{3-\delta}$ (LSF)	1.3 (± 0.12)	1 (±0.11)	(± S.D)
La$_{0.8}$Sr$_{0.2}$Co$_{0.8}$Fe$_{0.2}$O$_{3-\delta}$ (LSCF- 8282)	1.2 (± 0.05)	0.87 (± 0.05)	1.62 (± 0.38)
La$_{0.6}$Sr$_{0.4}$Co$_{0.2}$Fe$_{0.8}$O$_{3-\delta}$ (LSCF- 6428)	1 (± 0.12)	0.87 (± 0.11)	1.51 (± 0.32)
La$_{0.8}$Sr$_{0.2}$CoO$_{3-\delta}$ (LSC)	1 (± 0.1)	0.65 (± 0.12)	1.09 (± 0.25)

The exposed samples were powdered and analyzed by XRD.

Development of Reliability Model for OTM's

In developing a reliability model for the OTM it is necessary to know the behavior of flaws the material in response to its operating environment. Studies to understand the behavior of flaws, their initiation and propagation initial studies were done with flaws generated by Vickers indent. The cross sections of the indents were polished to reveal sub surface cracks beneath the indent. Of importance is the knowledge of the median crack. In the median-radial indentation crack system, the radial crack are shallow surface cracks and do not promote strength degradation. On the other hand, median crack propagate by further application of stress σ_{app} and can be related to the degradation in strength values. By characterizing the median crack, it is also possible to characterize the stress field around the flaw. The indentation load controls the length of the median crack, while the generation of the crack is by itself a function of the elastic properties of the indenter/material and the microstructure. The cross sections of LSCF 8282 and LSFCO indentation crack are shown in fig 2. In LSCF – 8282 (Fig 2a), the indentation load of 9.8 N produces a median-radial-lateral crack system and as reported in literature the fracture is intergranular. In LSFCO-2 (Fig. 2b) the indentation load of 9.8 N produces a median-radial-lateral crack system and according to our previous observations, fractures in a transgranular mode. In brittle solids, the lateral cracks are formed upon unloading the indentor and grow progressively from the median to the radial crack. Although, the lateral crack are not strength governing they interact with the radial crack and lead to a transition to damage mode of fracture. This corresponds to our observations that at higher loads (ex.: 9.8N), damage is seen around surface indents and result in increased scatter in measured hardness and toughness values.
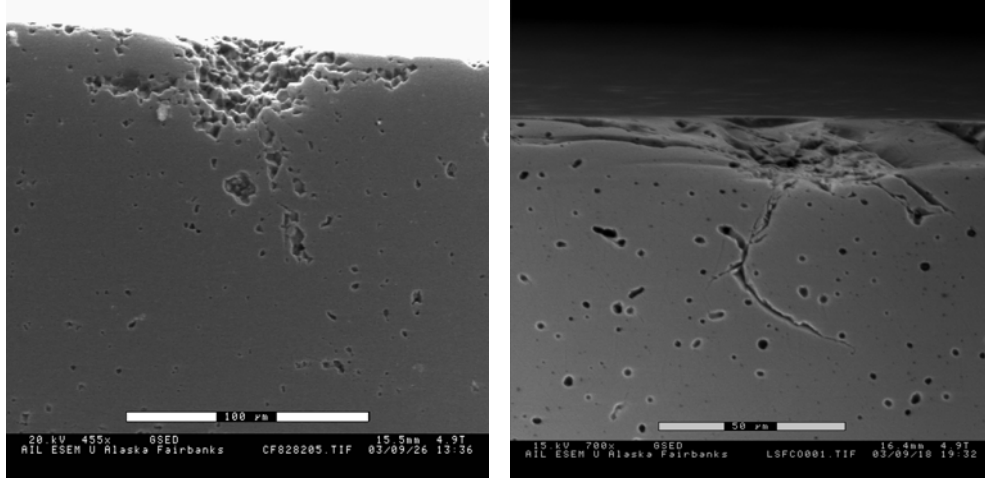
Fig. 2:   Crossection of an indent flaw formed at load P = 9.8 N in a) LSCF -8282
and b) LSFCO-2. Fracture in LSCF-8282 is intergranular as compared to
transgranular mode in LSCF)-2

The stress field around the median crack is linked to the indentation load by the relation:

$$\sigma_{ij} = \frac{P}{\pi R^2} f_{ij}(\varphi)$$ (1.2)

Where P is the indentation load, R the median crack length and the function f_{ij} relates the poisons ratio of the material, the angle to the crack to define the stress field around the indent. The radial (σ_{rr}), tangential ($\sigma_{\theta\theta}$) and shear forces (σ_{zz}, σ_{rz}) around the indent were calculated for LSFCO-2 assuming a Elastic modulus of 123 GPa and Poisson ratio of 0.22. Knowledge of these stresses, it is possible to compute the principal stresses σ_{11}, σ_{22} and σ_{33} respectively. The distribution of the stresses around the indent are shown in Fig. 3. In the next quarter, the element distribution around the median and radial surface crack will be studied and mapped.

 Initial attempts were also made to measure the crack tip parameters. As shown in fig.4, the crack opening displacements, *u(r)*, were measured behind the crack tip and related to the stress intensity for the linear-elastic median crack tip from the equation:

$$u(r) = \frac{K_{tip}}{E} \left[\frac{8(a-r)}{\pi} \right]^{\frac{1}{2}}$$ (1.3)

9
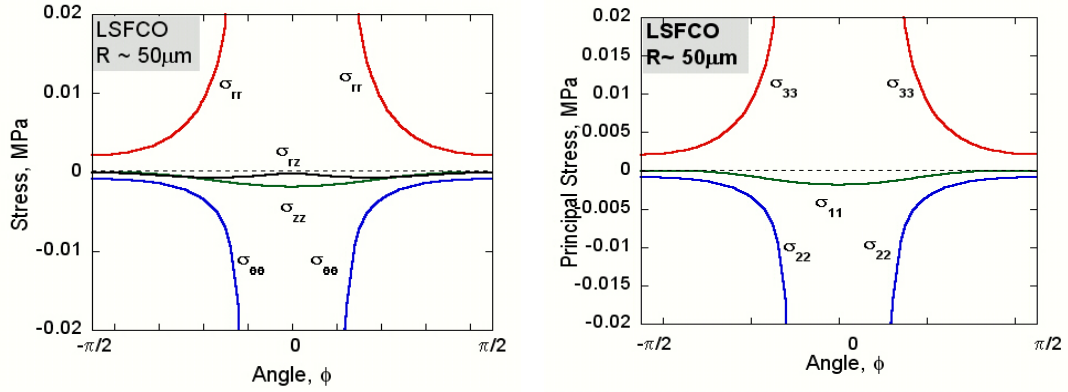
Fig. 3:   Stress fields around an indent flaw formed at load P = 9.8 N in LSFCO-2. The median crack was ~ 50µm as compared to ~100µm in LSCF-8282
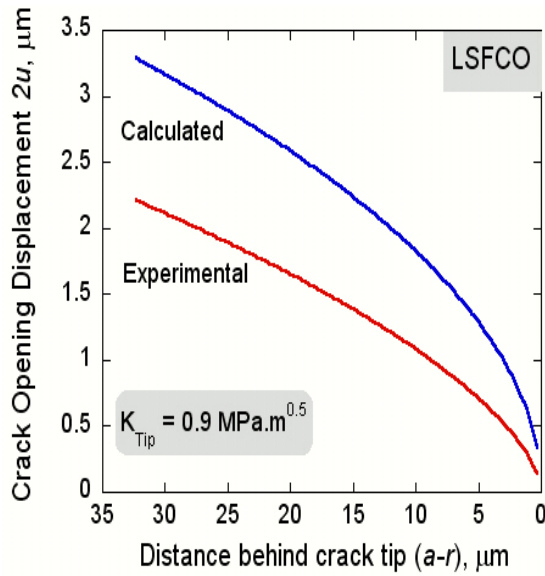
Fig. 4:   Crack opening displacement as a function of distance behind the crack tip. The profile provided a value of K_{tip} = 0.9 MPa.m$^{0.5}$

Where E= Young Modulus = 123 GPa, a is the crack length and r is the distance behind the crack tip. The stress intensity at the crack tip K_{tip} computed from the equation was 0.9 MPa√a. From the Von Mises criterion, σ^{max}, is given according to the equation:

$$\sigma^{max} = \frac{1}{\sqrt{2}}\sqrt{(\sigma_{11} - \sigma_{22})^2 + (\sigma_{22} - \sigma_{33})^2 + (\sigma_{33} - \sigma_{11})^2 + 6(\sigma_{12}^2 + \sigma_{13}^2 + \sigma_{23}^2)} \qquad (1.4)$$

An accurate description of the localized stresses and stress intensity are necessary for prediction of microscopic fracture origins such as stress induced segregational effects, precipitation etc.

Indentation flaw and residual stresses effects in La$_{0.2}$Sr$_{0.8}$Fe$_{0.8}$Cr$_{0.2}$O$_{3-x}$

Previous quarterly report had indicated that in some of the model MIEC perovskites studied, the crack lengths from starter indentation flaws were reduced after exposure to air at 1000ºC. This has an important bearing in evaluating crack growth parameters at elevated temperatures as the starting flaw is no longer what was characterized at room temperature. The flaw can interact with the environment get blunted or possibly grow some distance and thus affecting the crack calibrations.

To characterize and study the interaction of the cracks with the environment, the indents of LSFCO-2 was exposed to air at 1000ºC and also a complex schedule of heating in N$_2$ up t0 1000ºC prior to introduction of air. The latter schedule was recommended by researchers at Praxair and is designed to equilibrate the material prior to exposing it to air (the materials are fabricated by cooling in N$_2$).
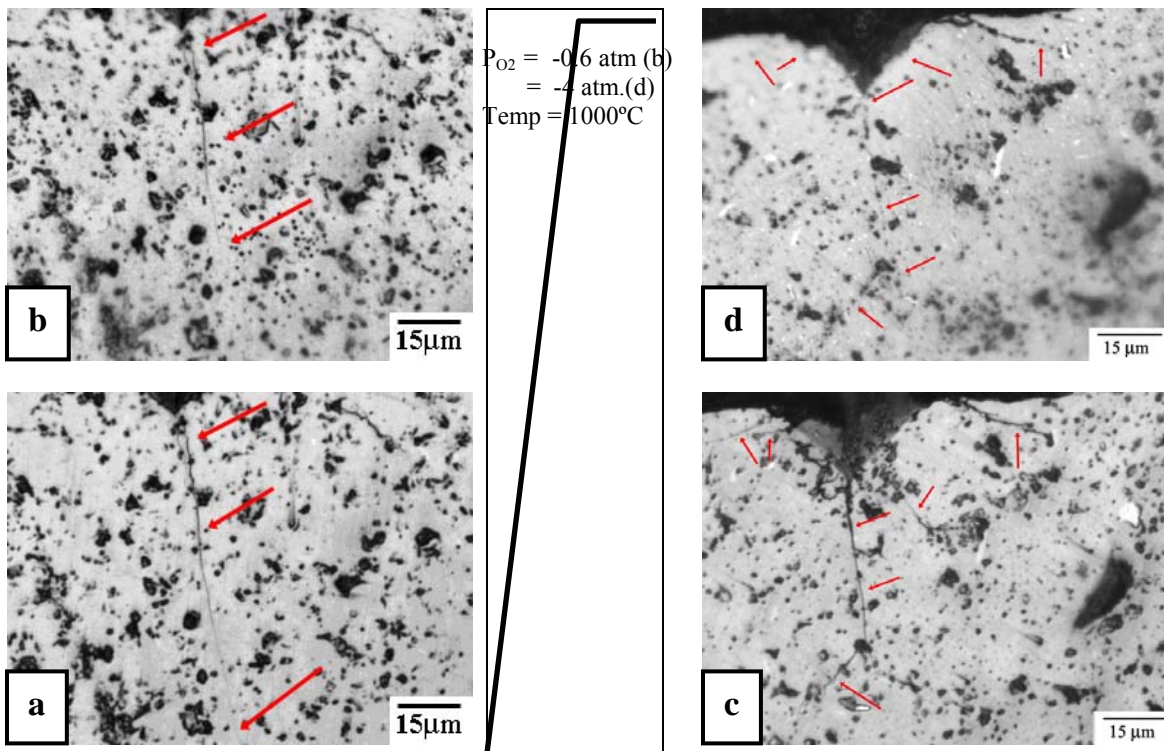

Figure 5:   An indented crack exposed to environment and elevated temperature shows reduction of radial crack lengths. a) In air at 1000ºC (P$_{O2}$ = -0.7 atm.) and b) in N$_2$/Air at 1000ºC (P$_{O2}$ = -4/-0.7 atm.)

Upon exposure to air at 1000ºC, the crack (Fig. 5b) in the indented flaws (10N) shows considerable reduction as compared to at room temperature (Fig. 5a). The reduction in crack length is more apparent when the indent is annealed in the environment of N_2 switched to air (Fig. 5 c and d).

In explaining the reasons, it can be argued that the reduction of the crack length is just the thermal relief from the tensile residual stresses. Since, the stress produced by the indent decreases with distance from the indent, the crack propagated by the applied stress (indentation load) will initially grow rapidly, then slows, and finally stops growing. Growth stops when the stress intensity K_I, drops to the critical stress intensity K_{Ic}. The effect of an applied stress is to change the length of the crack emanating from the indent. Tensile stress raise K_I value, increasing the crack length and conversely, a compressive stress shortens the crack. The compressive stress for closing the cracks can be derived by fracture mechanics based on the assumption that the crack grows until the stress intensity at the crack tip drops to K_{Ic}. The net stress intensity, which includes contributions from the residual stress at the indent and the stress σ_s present from other sources and closing the crack can be expressed as:

$$K_I = \chi_r \, P \big/ c^{3/2} + \sigma_a \Phi c^{1/2} \tag{1.5}$$

where χ_r is the residual stress parameter and ϕ is a parameter accounting for the geometry of the crack and c is the crack length.

Rearranging the equation and providing for the initial toughness and crack length as K_I (initial) and c_i respectively and the final crack length as c_f, the stress can be expressed as:

$$\sigma_S = (K_{Ic} - K_I(initial) c_i^{3/2} \big/ c_f^{3/2}) / \Phi c_f^{1/2} \tag{1.6}$$

Assuming that the crack system is half penny ($\phi = 0.30$) and there is no subcritical crack growth, the $K_{I,\,initial}$ and K_{Ic} can be assumed to be equal. The surface stress was calculated and is observed to be compressive.

In air: $\sigma_s \sim$ -7 MPa

In N_2/Air: $\sigma_s \sim$ -60 MPa.

The implication of these will be further analyzed during crack growth studies in four point flexure or C-ring geometry. Also studies are underway to evaluate the effect of thermal ageing in specified environment on the median crack.

Strength Degradation and slow crack growth studies:

In the present quarter, slow crack growth studies were begun on the new set of bar samples. The OTM samples termed LSFCO-3 were provided by Praxair in dimensions of 3x4x48 mm. Small samples were sectioned from one of the bar and analyzed for microstructure, phase composition, hardness and indentation toughness. As with studies on LSFCO-2 (tube), the indents on the polished samples were exposed to environment and the radial, lateral and median crack characterized. The results will be provided in the next quarterly report.
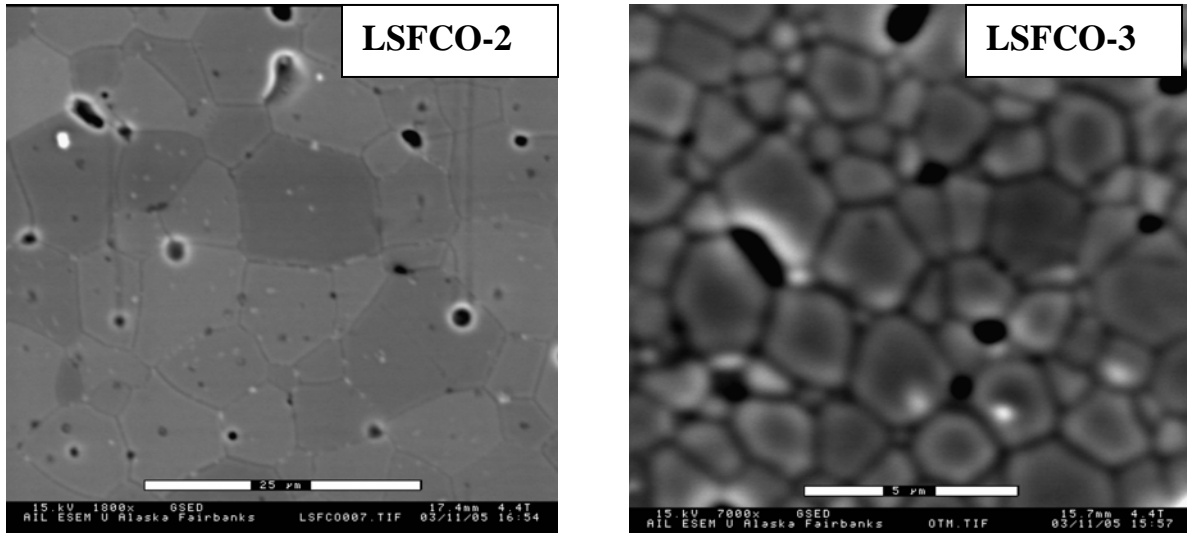
Figure 6:   Thermally etched microstructure of a) LSFCO-2 and b) LSFCO-3

The microstructure of LSFCO-3 (fig. 6a) was approximately ~ 3μm as compared to ~ 6μm in LSFCO-2 (fig. 6b). The average density of the LSFCO-3 samples as computed from volume measurements was approximately ~ . Some surface cracks were observed and was advised by Praxair as being shallow thermal relief cracks. The test samples were chamfered before testing in 4-point flexure.

Initial studies were done at room temperature. The samples were tested by monotonic loading in displacement control at 4 different crosshead speeds. The crosshead speeds of 3μm, 6μm, 60μm and 600μm were chosen so as to give a wide scale of loading spectrum. The fixture was unloaded immediately upon fracture and the fracture loads recorded.

The fracture strength of the bars were calculated from peak loads as:

$$\sigma_f = \frac{3Pl}{4bd^2} \qquad\qquad (1.7)$$

Where *P* is the fracture load, *l* is the outer support span = 38.1 mm, *b* is the specimen width and *d* is the specimen thickness.

The fracture strength of the bar tested at room temperature is as shown in Fig. 7.
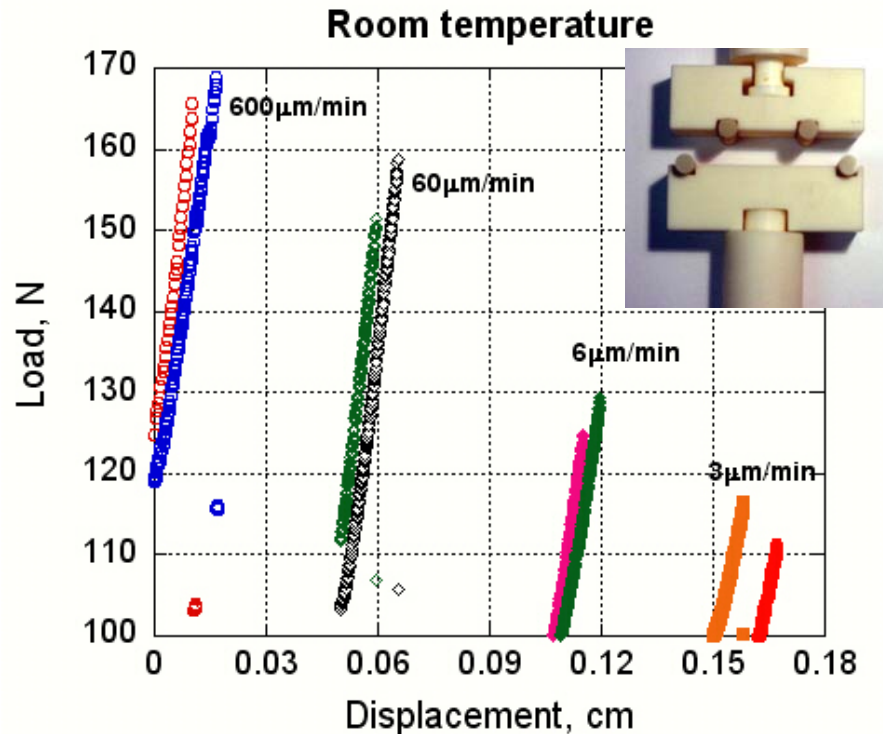
Figure 7:　　　Load-displacement trace of OTM bars test in flexure at varying strain rates.

Slow crack growth at room temperature appeared to be a probable reason for the changes in strength values. This will be characterized by plotting the fracture strength as a function of stress or strain rates calculated from individual tests. Extensive fractographic evidence on fracture origin, slow crack growth will be collected and analyzed in the next quarter.

CONCLUSIONS

The progress of the task on mechanical properties in chemical environment is on several fronts: a) fundamental understanding and b) studies for the practical applications. In this quarter, indent flaws in OTM and other MIECs were characterized upon exposure to specific environment. The new sets of materials provided by Praxair were evaluated for room temperature strength as a function of strain rates.

Task 3:   Preparation and Characterization of Dense Ceramic oxygen Permeable Membranes

X.-D Zhou, Y.-W. Shin, and H. U. Anderson

Electronic Materials Applied Research Center, Department of Ceramic Engineering, University of

Missouri-Rolla, Rolla, MO 65401

The search for the new generation of the oxygen transport membrane materials and understanding the mechanisms for oxygen vacancy generation and oxygen reduction are of great importance in order to increase the energy efficiency and improve the national energy security [1, 2]. One technique to improve the materials properties is to tailor its microstructure, for example its porosity, tortuosity, composite connectivity etc; the other technique is to design the cathode to be mixed ionic and electronic conductor (MIECs) [3]. Lanthanum ferrites ($La_{1-x}Sr_xFeO_3$, LSF) are being considered as the favorite oxygen transport membrane materials and of particular interest in the fundamental and practical research, partly because this series possesses a wide range of solid solutions from x = 0 to x = 1. In addition, it was found that A site deficient LSF was a thermodynamic stable phase. This report includes (1) the electrical conductivity measurements on $La_{0.55}Sr_{0.35}FeO_3$, an A site deficient compound and (2) electrical conductivity measurements of A site stoichiometric $La_{0.60}Sr_{0.40}FeO_3$ and $La_{0.80}Sr_{0.20}FeO_3$.

1   Experimental

The modified Pechini method was used to synthesize nanocrystalline particles, which were calcined at various temperatures to prepare powders. Bar shaped specimens (3.8 cm x3mm x3mm) were prepared for electrical measurements by uniaxial-pressing at 40 MPa, followed by cold isostatic pressing at 310 MPa. Bars were sintered on LSF substrates of the same composition at temperatures ranging between 1000 to 1400°C, with a heating rate of 3°C/min and a soak time of 4 h. Scanning electron microscopy (Hitachi S-4700 and JEOL T330A, SEM) was used to investigate the raw materials and sintered ceramics.

A four-point dc method was used to measure electrical conductivity using a Solartron 1260 frequency response analyzer with a 1296 interface. Thick film Pt electrodes (Electro-Science Lab, 9912-G) were used for all measurements. Data were collected for temperatures ranging between 200 and 1200°C. All electrical measurements were performed only after a stable value of the dc conductivity was achieved.

3. Results and Discussion

3.1 Electrical Conductivity Measured in Air

Electrical conductivity (σ) is determined by carrier concentration (N), carrie mobility (μ) and charge of the carrier (q) as:

$$\sigma = N\mu q$$

Carrier concentration in LSF system is dependent on acceptor dopant level ($[Sr_{La}']$ and oxygen vacancy density ($[V_O^{\bullet\bullet}]$) as:

$$N = [Sr_{La}'] - 2[V_O^{\bullet\bullet}].$$

In LSF system, the carriers are also considered as Fe^{4+} locating at Fe^{3+} sites. Therefore, carrier concentration can also be calculated from Fe valence state. For example, the average Fe valence state is 3.4 in $La_{0.60}Sr_{0.40}FeO_3$ (L6SF) thus the carrier density would be 40% of total Fe sites. It will be straightforward to achieve carrier density as 20% in $La_{0.80}Sr_{0.20}FeO_3$ (L8SF) and 65% in $La_{0.55}Sr_{0.35}FeO_3$ (L55SF).[4] A highest electrical conductivity is expected in $La_{0.55}Sr_{0.35}FeO_3$ because of the highest carrier concentration. Fig. 1 shows plots of electrical conductivity of these three compounds measured in air from 200 to 1200°C. The results from Fig. 8 are twofold: (1) the electrical conductivity mainly is determined by carrier concentration in the measuring temperature regime as ($\sigma_{L8SF} < \sigma_{L6SF} < \sigma_{L55SF}$) (2) there exists a maximum conductivity for each compound at a different temperature.

Fig. 9 are plots of $\ln(\sigma T)$ vs. $1/T$ for L8SF, L6SF and L55SF. A small polaron conduction was proposed in these p type conductor systems, such as chromites, manganate, and cobaltites. The mobility term can be achieved over the regime where $\ln(\sigma T)$ is linearly proportional to $1/T$ (Table 2). Mobility values are similar for the compounds in this study, indicating the similar conduction mechanism in ferrite system. Co doped ferrites, however possess a much lower mobility, thus LSCF often has a higher conductivity value than LSF.
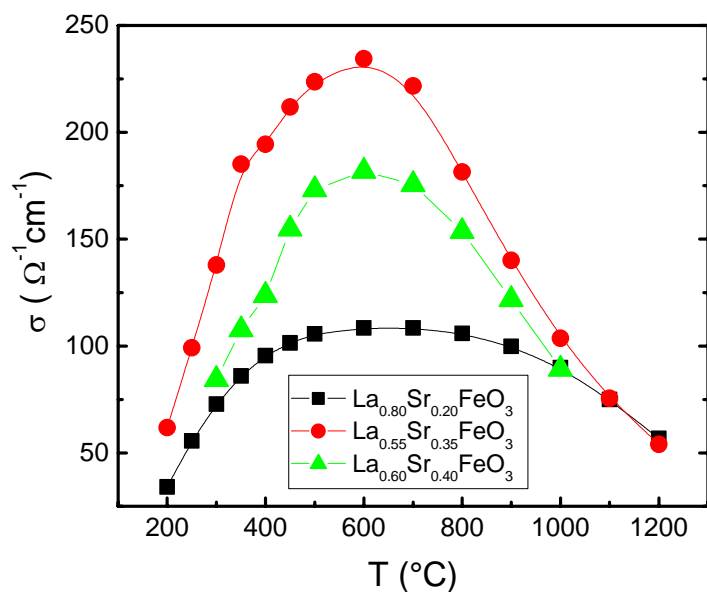
Fig. 8.   A plot of conductivity (σ) vs. temperature (°C) for $La_{0.80}Sr_{0.20}FeO_3$, $La_{0.60}Sr_{0.40}FeO_3$ and $La_{0.55}Sr_{0.35}FeO_3$ measured in air.
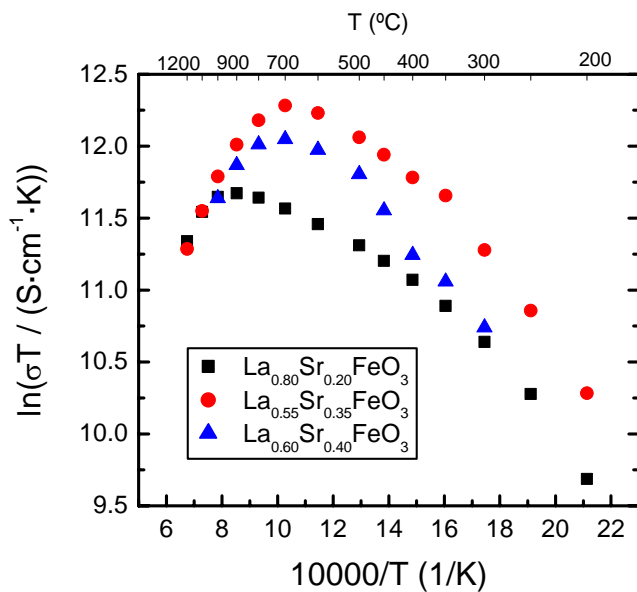
Fig. 9.   A plot of conductivity ln(σT) vs. 1/T for $La_{0.80}Sr_{0.20}FeO_3$, $La_{0.60}Sr_{0.40}FeO_3$ and $La_{0.55}Sr_{0.35}FeO_3$ measured in air. Activation energy can be calculated from the slope over relative low temperature regime (200 – 500°C)
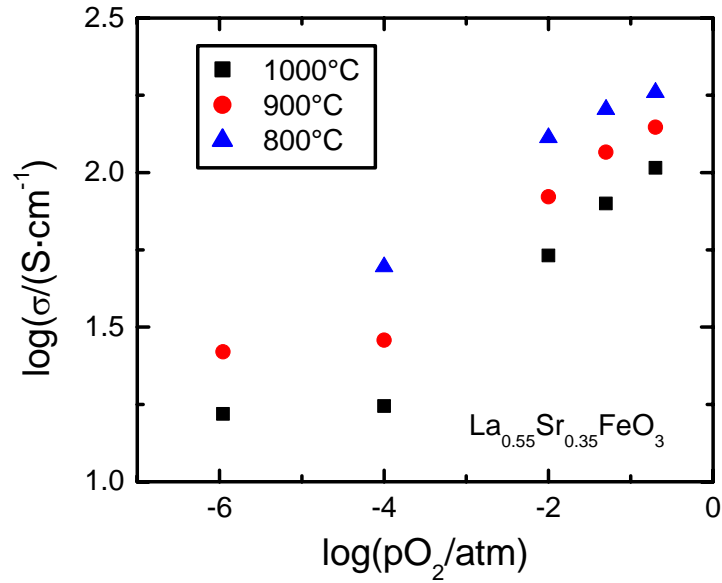
Fig. 10.   A plot of log(σ) vs. log(pO_2) for $La_{0.55}Sr_{0.35}FeO_3$ at various oxygen activities at 1000, 900 and 800°C.

Table 2. Activation for mobility of LSF and LSCF

	$La_{1-x}Sr_xFeO_{3-\delta}$			$La_{1-x}Sr_xFe_{0.80}Co_{0.20}O_{3-\delta}$			
	x=0.2	x=0.4	L55SF	x = 0.4	x = 0.3	x = 0.2	x = 0.1
E_h (eV)	0.28	0.24	0.23	0.087	0.13	0.16	0.18

The maximum in conductivity represents the temperature at which the oxygen vacancy concentration starts to influence the carrier concentration. It does not mean that the oxygen vacancy concentration is negligible at this temperature, but on the other hand, the influence of oxygen vacancy concentration on total carrier concentration is negligible below this temperature and the concentration of oxygen vacancies is so small that their contribution to transport processes becomes minimal. Since oxygen vacancies are required for lower cathodic overpotentials, this temperature also represents the temperature below which a cathode can be expected to have high overpotentials.

3.2 Oxygen Activity Dependence of the Electrical Conductivity

Oxygen activity dependence of the electrical conductivity of L55SF is shown in Fig. 10. Equilibrium is very easy to achieve (several hours) when oxygen partial pressure is higher than 10^{-2} atm. A much long equilibrium time is required for measuring stable conductivity value when pO_2 is less than 10^{-3} atm (normally ~ couple of days). At 800°C, when pO_2 was 10^{-6} atm, the sample was not at equilibrium state even after a week. The conductivity leveled out for 1000 and 900°C, when the pO_2 decreased below 10^{-4} atm. Similar behavior has been observed for other compounds in LSF series at relatively low temperature (< 900°C).

TASK 4:   Assessment of Microstructure of the Membrane Materials to Evaluate the Effects of vacancy-Impurity Association, defect Clusters, and Vacancy Dopant Association on the Membrane Performance and Stability

Professor Nigel Browning, University of Illinois Chicago Circle

EXPERIMENTAL

The key to obtaining detailed information on the structure, composition and bonding at interfaces and defects is linked to the ability of the STEM to form a small electron probe. Figure 13 shows a schematic of the detector arrangement in the STEM demonstrating that all the signals of interest for materials characterization can be acquired simultaneously, relative to the probe position on the surface of the sample. The starting point for the analysis is the Z-contrast image, which is formed by collecting the high-angle scattering on an annular detector (Figure 1). Detecting the scattered intensity at these high-angles and integrating over a large angular range effectively averages coherence effects between neighboring atomic columns in the specimen. Thermal vibrations reduce the coherence between atoms in the same column to residual correlations between near neighbors, a second order effect. This allows each atom to be considered as an independent scatterer. Scattering factors may be replaced by cross sections, and these approach a Z^2 dependence on atomic number. This cross section effectively forms an object function that is strongly peaked at the atom sites, so for very thin specimens where there is no dynamical diffraction, the detected intensity consists of a convolution of this object function with the probe *intensity* profile (Figure 13). The small width of the object function (~0.02 nm) means that the spatial resolution is limited only by the probe size of the microscope. For a crystalline material in a zone-axis orientation, where the atomic spacing is greater than the probe size, the atomic columns are illuminated sequentially as the probe is scanned over the specimen. An atomic resolution compositional map is thus generated, in which the intensity depends on the average atomic number of the atoms in the columns.

This result also holds true for thicker specimens. In this case, the experimental parameters cause dynamical diffraction effects to be manifested as a columnar channeling effect, thus maintaining the thin specimen description of the image as a simple convolution of the probe intensity profile and an object function, strongly peaked at the atom sites. The phase problem associated with the interpretation of conventional high-resolution TEM images is therefore eliminated.   In thin specimens, the dominant contribution to the intensity of a column is always its composition. However, due to the higher absorption of the heavy strings the contrast does decrease with increasing specimen thickness and in very thick crystals there is no longer a high resolution image. The effect of changing focus is also intuitively

understandable as the focus control alters the probe intensity profile on the surface of the specimen. For defocus less than the optimum Scherzer condition, the probe broadens causing the individual columns not to be resolved. For higher defocus values the probe narrows with the formation of more intense tails, causing sharper image features but compositional averaging over several columns. The optimum focus condition therefore represents a compromise between high resolution (narrow probe profile) and the desire for a highly local image (no tails to the probe). This focus condition also corresponds to the optimum probe for microanalysis.
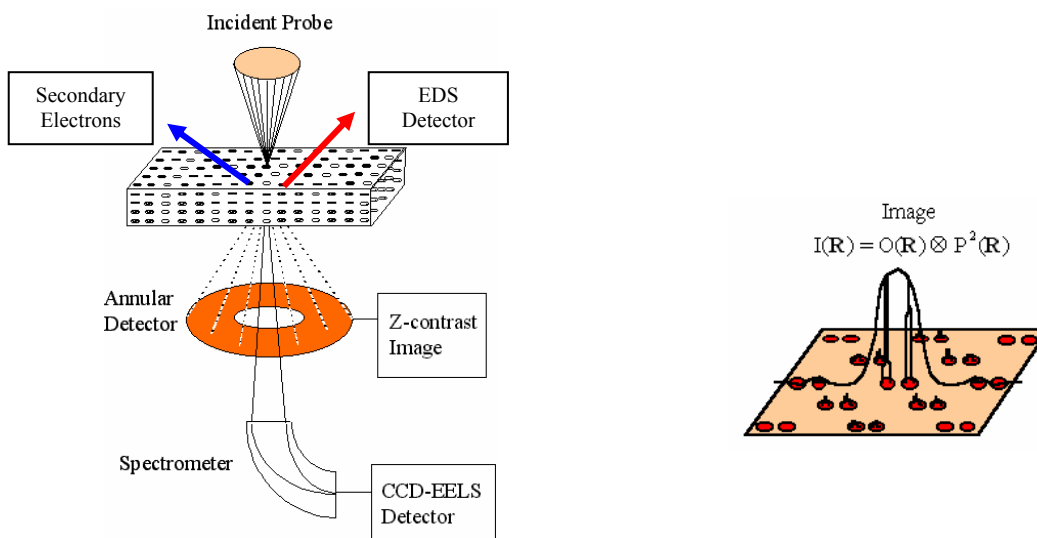

Figure 11: (a) Schematic of the STEM. (b) The Z-contrast image and energy loss spectrum can be interpreted as a simple convolution of the experimental probe and the object function. With lower spatial resolution, the EDS spectrum can also be interpreted in this manner.

As can be seen from Figure 13, the annular detector used for Z-contrast imaging does not interfere with the low-angle scattering used for EELS. This means that the Z-contrast image can be used to position the electron probe over a particular structural feature for acquisition of a spectrum. The physical principle behind EELS relates to the interaction of the fast electron with the sample to cause either collective excitations of electrons in the conduction band, or discrete transitions between atomic energy levels, e. g. 1s 2p transitions. The ability to observe discrete atomic transitions allows compositional analysis to be performed by EELS (the transitions occur at characteristic energy losses for a given element). Furthermore, the transitions to unoccupied states above the Fermi level allows the degree of hybridization between atomic orbitals to be determined, i.e. information on local electronic structure (bonding) changes can be ascertained. To be able to correlate these features of the spectrum precisely with a structural feature of interest, it is essential that the spectrum have the same atomic resolution as the

21

Z-contrast image. In order to achieve this atomic resolution, the range over which a fast electron can cause an excitation event must be less than the inter-atomic spacing. Hydrogenic models show that for the majority of edges accessible by conventional energy-loss spectrometers. E < 2 keV) the object functions are localized within 0.1 nm of the atom cores. Hence, like the Z-contrast image, we have an object function localized at the atom cores and an experimental probe of atomic dimensions. For crystalline materials in zone-axis orientations, providing we maintain a large collection angle, the description of the spectrum (Figure 1) in terms of a convolution of the probe with an object function is valid.

In this quarter, there was no significant progress made caused mostly by sample breakage and problems with microscope contamination (one of the unfortunate side effects of this level of microscopy).

Task 5: **Measurement of Surface Activation/Reaction rates in Ion Transport Membranes using Isotope Tracer and Transient Kinetic Techniques.**

Prof. Alan Jacobson, University of Houston/University of Toronto

EXPERIMENTAL

University of Houston

Conductivity and Thermodynamic Studies

We have continued to investigate the thermodynamic properties (stability and phase separation behavior) and total conductivity of prototype membrane materials. The data are needed together with the kinetic information to develop a complete model for the membrane transport. We have previously reported initial measurements on a sample of $La_{0.2}Sr_{0.8}Fe_{0.55}Ti_{0.45}O_{3-x}$ prepared in-house by Praxair. Subsequently, we have received a second sample of powder from a larger batch of sample. We have characterized this material and compare the results with the previous batch.

X-ray diffraction and microprobe analysis

The $La_{0.2}Sr_{0.8}Fe_{0.55}Ti_{0.45}O_{3-x}$ powder was calcined at a series of temperatures (1250 ºC, 1300 ºC and 1400 ºC in air to investigate phase purity and densification behavior. The X-ray data are shown in Figure 12. The sample is apparently single phase after heating at 1250 ºC though some line broadening is apparent. At 1400 ºC the lines become sharper and the pattern can be completely indexed with a tetragonal unit cell with lattice parameters a = 5.523(7) Å and c = 7.811 Å (cf. 5.506(9) Å and 7.787(9) Å for batch#1 sintered at 1300 ºC). The density measured by the Archimedes method was 90% of the theoretical value after annealing the sample for 10 h at 1400 ºC.
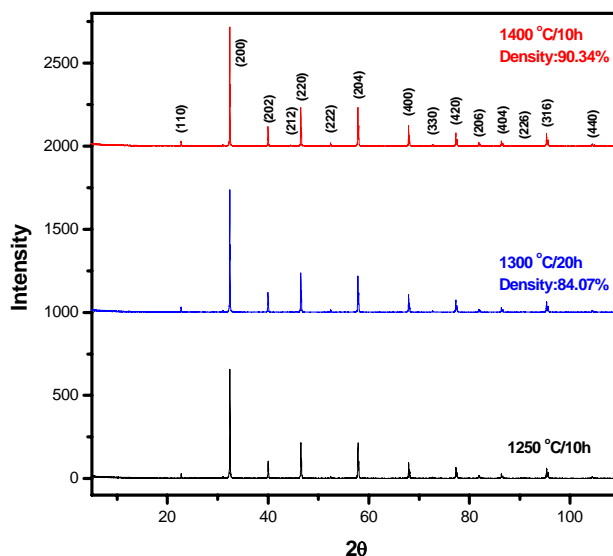
Figure 12. X-ray diffraction data for $La_{0.2}Sr_{0.8}Fe_{0.55}Ti_{0.45}O_{3-x}$ samples annealed at different temperatures – batch #2.

Samples were mounted and polished for electron microprobe analysis using a JEOL JXA-8600 Electron Microprobe. Elemental compositions were determined with the probe placed at different spots on the sample and the composition ratios determined from the average data to be La : Sr = 0.2 : 0.80 and Fe : Ti = 0.55 : 0.45 in agreement with the nominal composition. Some small variations in composition were observed in most part due to the roughness of the sample surfaces.

Table 3. The composition of $La_{0.2}Sr_{0.8}Fe_{0.55}Ti_{0.45}O_{3-x}$ batch #2

Point	Atomic %				
#	La	Sr	Fe	Ti	O
1	3.948	16.104	11.567	9.412	58.970
2	3.961	16.522	11.695	9.475	58.348
3	3.977	16.338	11.560	9.615	58.510
4	3.979	16.181	11.673	9.553	58.614
5	4.021	16.331	11.749	9.634	58.265
Average	3.977	16.295	11.649	9.538	58.541
S. D.	0.028	0.161	0.083	0.094	0.276
Composition	0.196	0.804	0.550	0.450	3.00-x

A rectangular bar with dimensions $0.90 \times 0.25 \times 0.19$ cm was cut from the sample that was sintered at 1400 °C. Conductivity measurements were made as a function of temperature in different gas atmospheres by the four-probe dc method. Gold wires were used as electrodes and measurements were made on both heating and cooling to ensure that equilibrium had been attained. The results are shown in Figure 13.
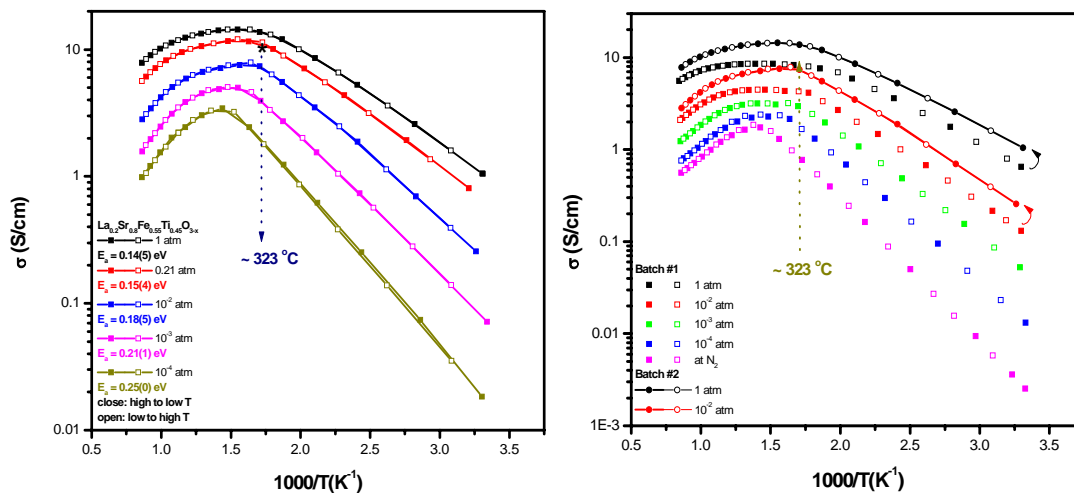
Figure 13. DC conductivity data for $La_{0.2}Sr_{0.8}Fe_{0.55}Ti_{0.45}O_{3-x}$ in different gas atmospheres as a unction of reciprocal temperature (left batch #2). The right hand figure is a comparison of data for batch #1 and batch #2 (solid lines).

The results are typical for perovskite materials and are similar for the two batches. The conductivity shows Arrhenius behavior at temperatures lower than about 300 °C. The activation energy increases with decreasing oxygen partial pressure as the contribution from ionic conductivity to the total conductivity increases. The maximum conductivity observed in pO_2 = 1 atm is ~10 S cm^{-1} and is significantly higher for batch #2. Above 300 °C, the conductivity falls as the oxygen stoichiometry increases because of the relationship $[Sr^{'}] = [h^{\bullet}] + 2[V^{\bullet\bullet}]$. At the higher oxygen pressures, the plateau observed in the conductivity for the batch #1 sample is not observed for batch #2.

A rectangular bar with dimensions $0.29 \times 0.18 \times 1.03$ cm was cut from the sample sintered at 1400 °C. Measurements were made in a sealed electrochemical cell as a function of oxygen partial pressure at temperatures from 750 °C to 1000 °C down to 10^{-17} atm for the lowest temperature. The measurements were made using an ac technique at a single frequency and the phase angle monitored to confirm the absence of any polarization effects. Measurements were made on both decreasing and increasing pO_2 and the results are shown in Figure 14.
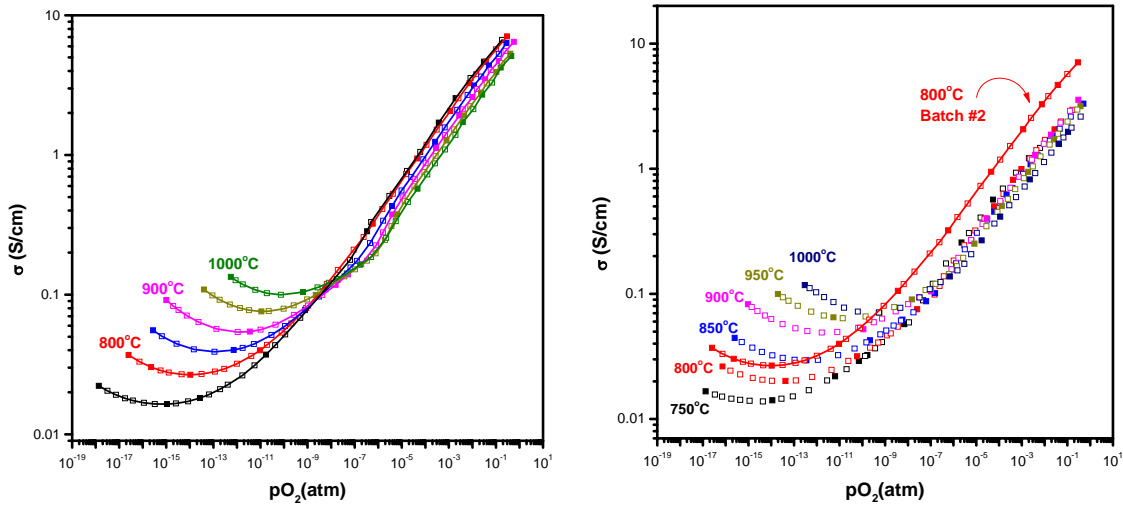
Figure 14.   Conductivity measurements for $La_{0.2}Sr_{0.8}Fe_{0.55}Ti_{0.45}O_{3-x}$ (batch #2)as a function of pO_2 at different temperatures. Open and closed symbols represent data taken on increasing and decreasing pO_2. The right hand figure shows a comparison of the 800 °C data (solid line) with the previous batch #1 data.

The data are typical for perovskite oxides. The conductivity initially p type at high oxygen partial pressure decreases as pO_2. The slope of the linear region in a log –log plot is ~1/4 as expected. Little temperature variation is seen in this region presumably because the decrease in hole conductivity associated with oxygen loss is offset by an increase in the ionic conductivity. As the pO_2 is further decreased, the conductivity goes through a minimum and then becomes n type with a $pO_2^{-1/4}$ dependence. In general, the system is well behaved with little evidence for problems in attaining equilibrium that we have found in the other iron systems that we have studied. The p to n transition is well defined at all temperatures.

The pO_2 dependence of the conductivity data for $La_{0.2}Sr_{0.8}Fe_{0.55}Ti_{0.45}O_{3-x}$ were further analyzed as before using a simple model that expresses the total conductivity as the sum of the ionic conductivity and the p and n type contributions according to:$\sigma_T = A + B \times pO_2^{1/4} + C \times pO_2^{-1/4}$. This simple model fits the data well (see Table 4) though it does not take proper account of the behavior in the p type region where changes in the stoichiometry effect the ionic conductivity (by changing the vacancy concentration) in addition changing the hole contribution. The two off setting effects lead to an apparent near zero activation energy (see Figure 15).

26

Table 4.   Results from the model fit to the pO$_2$ dependence of the total conductivity data

La$_{0.2}$Sr$_{0.8}$Fe$_{0.55}$Ti$_{0.45}$O$_{3-x}$	A	B	C
750 °C	0.0128	11.529	3.42×10^{-7}
800 °C	0.0204	11.037	1.13×10^{-6}
850 °C	0.0265	9.147	3.85×10^{-6}
900 °C	0.0347	7.635	1.00×10^{-5}
950 °C	0.0453	6.543	3.00×10^{-5}
1000 °C	0.0527	6.003	7.00×10^{-5}

Nevertheless, reasonable values for the ionic conductivity are derived ~0.03 Scm^{-1} with an apparent activation energy of 0.63 eV, closely similar to the results obtained for batch #1.
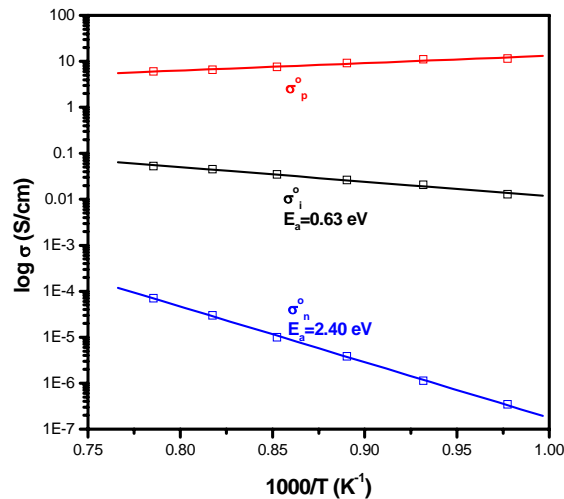
Figure 15. The individual contributions to the total conductivity of La$_{0.2}$Sr$_{0.8}$Fe$_{0.55}$Ti$_{0.45}$O$_{3-x}$ (batch #2).

University of Toronto

Isotope Transient Studies of Oxygen Permeation Through a Dense La$_{0.6}$Sr$_{0.4}$Co$_{0.2}$Fe$_{0.8}$O$_{3-\delta}$ Membrane

Summary of experimental progress:

(1) We concluded our investigations of oxygen transport properties through a dense La$_{0.6}$Sr$_{0.4}$Co$_{0.2}$Fe$_{0.8}$O$_{3-\delta}$ (LSCF) membrane under various conditions.

- A brief investigation of the influence on oxygen flux of water vapor on the air side was performed 850 ˚C.

27

- A final isotope transient at steady state was performed and was quenched during the evolution of the transient and the isotope profile measured.

(2) We have installed a membrane of $La_{0.2}Sr_{0.8}Cr_{0.2}Fe_{0.8}O_{3-\delta}$ (LSCrF) and begun air permeation measurements, to be followed by syngas components on the delivery side.

Influence of water vapor

The impact of water vapor in the air side of the membrane is presented in Fig. 16. The oxygen flux remarkably decreased with time during the first three days and stabilized after seven days.
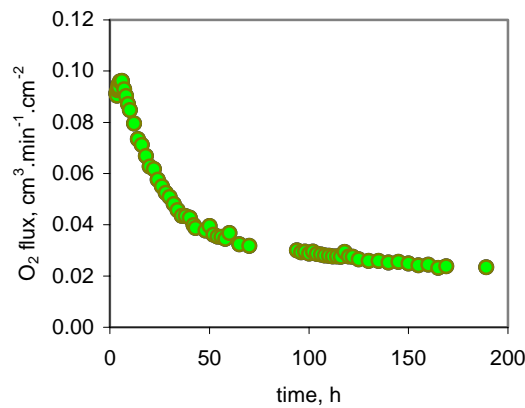

Figure 16.   Variation of the oxygen flux as a function of time with water vapor (28.6% or 286 mbar) at the air side under the following conditions: 850 ˚C, air side gas 20% O_2/28.6% H_2O /N_2 = 20 ml/min, sweep side gas He = 25 ml/min.

The change was largely irreversible and therefore can not be solely attributed to the reversible formation of hydroxy groups by the reaction water molecules with vacancies in the lattice:

$$V_O^{\bullet\bullet} + H_2O + O_O^x = 2[OH]_O^{\bullet}$$
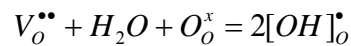
During this treatment, leaks from the air side to the sweep side became larger, indicating structural changes to the membrane. The leak was not so large as to preclude the final experiment; the quenching of the membrane during an isotopic transient

Quenched isotopic transient

In the past 6-9 months, we have been performing isotopic transients on an LSCF operating membrane. The time dependence of ^{18}O isotope after a short pulse of $^{18}O_2$ delivery to the air side reveals much about the transport in the membrane during steady state. As shown in the last quarterly

report, the values of the surface and bulk transport parameters can be individually assigned, including the reversibility of oxygen activation at the air side surface. During the last quarter, we quenched the LSCF membrane during the evolution of an isotopic transient, sectioned the tube and analyzed the ^{18}O distribution in the membrane.

After introducing a 15 min 20%$^{18}O_2$/Ar pulse, the sample was quickly cooled by opening the split-shell furnace. The temperature drop to 650 ºC required only 5 minutes – a small time compared to the evolution of the isotopic transient (almost one day). The compression on the gold seals was released during the cooling, and the air leak rate increased, especially in the temperature range 400-600 ºC. Part of this leak was due to the sample cracking

The sample was glued together before it was encased into a stainless-steel tube. Epoxy resin mixed with electrically conductive powder was for this and for the encasement of the sample inside the steel tube. The encased sample was cut by a diamond saw at two locations to expose cross-sections of the tubular sample. One cut was near the middle of the membrane and the other 1mm from the top of the tube. The cross-sections were polished to 0.25 micron. The surface was cleaned by Ar^+ sputtering in the ToFSIMS chamber before the measurements of the ^{18}O fraction by ToFSIMS imaging. Figure 19 shows the image obtained on the exposed profile in the middle of the sample.

The SIMS image shows that *O fraction varies with angle, indicating substantial heterogeneity in the sample. Approximately a factor of two is seen in the peak isotope fraction with angle. Some of this heterogeneity may have been induced by the water vapor treatment. The isotope fraction shows a hot spot in the upper part of the image which is close to a crack in the removed sample. This region was probably associated with a weak spot or incomplete crack in the sample. Other cracks in the removed sample do not show unusual isotope composition, indicating that they were induced largely by the thermal shock during cooling. The radial distribution at each angular region can be analyzed to obtain local surface and bulk mobilities. This work is in progress.

It should be noted that we increased the sweep gas (He) flow rate from 20 to 200 ml.min^{-1} in order to get a higher oxygen chemical gradient across the membrane. After the water experiment, the gas composition at the sweep side is 3.1% N_2 / 1.2% O_2 /He when the He flow is at 20 ml.min^{-1}, which indicates a leak rate of O_2 is 0.2 cm^3.min^{-1}.cm^{-2}. The oxygen partial pressure at the sweep side (P_{O2}'') changed to 0.14% (1.4 mbar). The low P_{O2}'' achieved minimized the surface exchange of leaked $^{18}O_2$ on the sweep side during the transient.
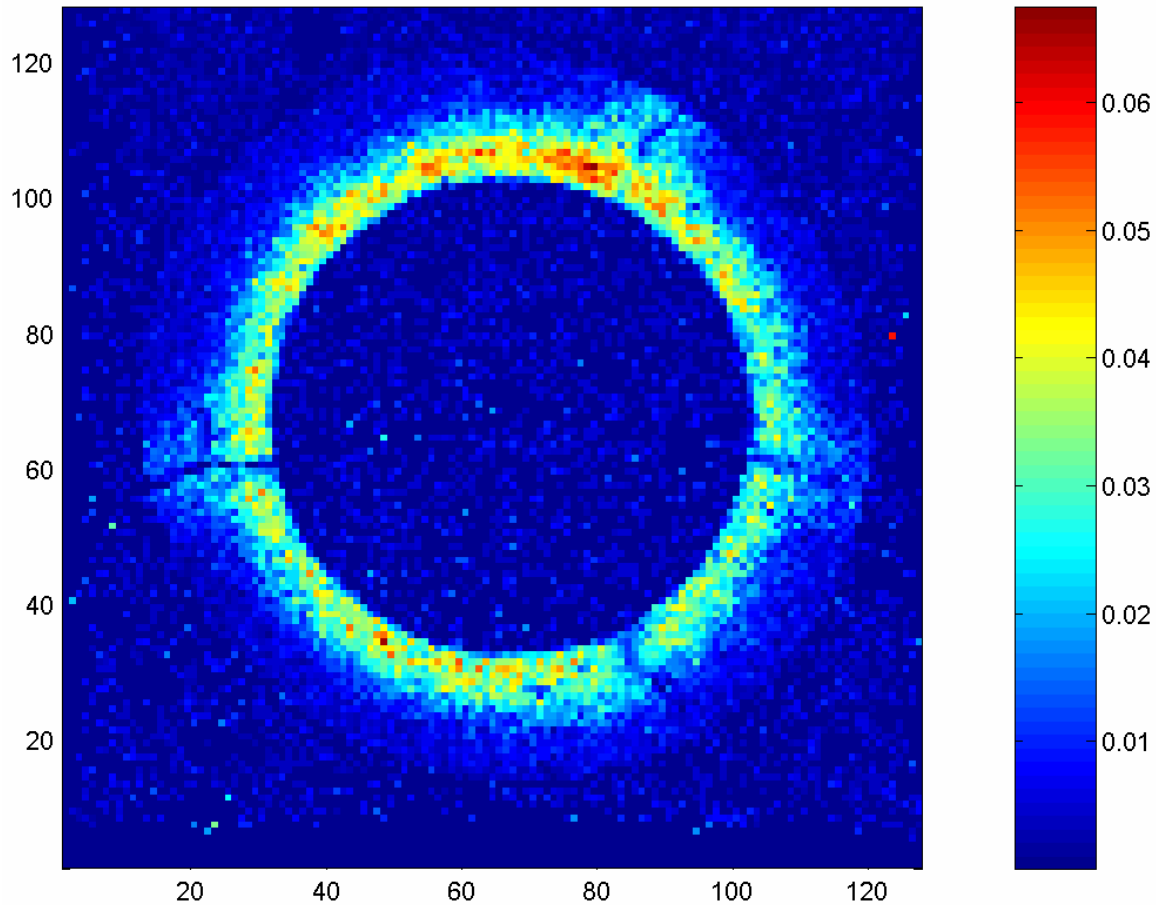
Figure 17.   An image of *O fraction distribution at one cross-section of the quenched sample (128x128 pixels). The color bar shows the scale of *O fraction

Preliminary measurements show similar behavior at the cross-section near the end of the membrane. No anomalies were associated with the tabs of the gold seal.

Installation of LSCrF membrane:

We have installed a new sample $La_{0.2}Sr_{0.8}Fe_{0.8}Cr_{0.2}O_{3-x}$ into the reactor. The first tube during heatup, but the second is now functioning as an air separation membrane with He sweep at 900⁼C. Good seals have been obtained – currently there are no detectable leaks in the current membrane.

Plans for the next quarter:

(1) *Analysis of LSCF data:* Many isotope transients obtained during the past six months on the second of our LSCF membranes indicated that there were heterogeneities in the membrane.

Although generally acceptable fits of the isotope transients could be obtained with the one dimensional constant properties model, there were unresolvable differences between the shapes of the fits and the data. This is in contrast with the previous sample, where excellent fits to the entire transient were obtained. The ToFSIMS results above showing clear inhomogeneities in this membrane, some of which were introduced by the water treatment, are consistent with this observation. Some of the heterogeneity undoubtedly existed in the original membrane. The ToFSIMS images will be acquired with better signal/noise ratios and analyzed for local agreement with the simple 1-D constant properties model. The distribution of contributions of fast and slow areas will be calculated and applied to improve the interpretation of the previous data.

(2) *LSCrF experiments:* The new LSCrF membrane will be briefly examined as it functions as an air separation membrane. Isotopic transients will be measured at membrane steady state, and the values of surface and bulk transport parameters obtained in the same manner as for LSCF. The flux dependence on the He sweep rate will be briefly measured. If sufficient variation is noted, isotopic transients will be performed at both high and low sweep rates to determine the variation in transport parameters at low and more severe oxygen potential gradients. After this, a CO/CO_2 mixture will be introduced, the oxygen flux measured. Isotopic transients will be measured in various situations. The isotope response involves exchange between CO_2 and the surface. Oxygen isotope appearance in CO will signal the reversibility of CO oxidation. Other atmospheres such as H_2/CO_2 will also be measured to test the relevant oxidation rates on the fuel side of this membrane. By the next quarterly report, we hope to have the first "syn-gas" condition isotope transients measured and partly analyzed.

CONCLUSIONS

A better model for the thermochemical interactions between Zirconia layers and Ti thin films allows a better estimation of the processing times necessary to obtain a stable interface in perovskite/metal applications where Zirconia-based diffusion barriers are used to decrease the interaction between the TLPB alloy and the substrate itself. Furthermore, the model develop in this work may eventually be applied to describe the detrimental liquid metal/perovskite interactions that prevent the creation of reliable perovskite/metal interfaces without the use of protective diffusion barriers.

The progress of the task on mechanical properties in chemical environment is on several fronts: a) fundamental understanding and b) studies for the practical applications. Earlier studies have pointed to the importance of characterizing the interaction between flaws and the environment in developing a failure analysis model. The present work provides information on crack tip stresses and stresses around indent flaws in OTM and other MIECs. Studies on slow crack growth provide quantitative effect of time and the effect of environment on characterized flaws. The logical step is to evaluate the effect of environment in a step fashion beginning in a environment of N_2/Air.

The oxygen activity dependence of the electrical conductivity of L55SF indicates that equilibrium is very easy to achieve (several hours) when oxygen partial pressure is higher than 10^{-2} atm. A much long equilibrium time is required for measuring stable conductivity value when P_{O2} is less than 10^{-3} atm (normally ~ couple of days). The conductivity leveled out for 1000 and 900°C, when the P_{O2} decreased below 10^{-4} atm. Similar behavior has been observed for other compounds in LSF series at relatively low temperature (< 900°C). This needs to be further investigated in other complex membranes.

Studies of the $La_{0.2}Sr_{0.8}Fe_{0.55}Ti_{0.45}O_{3-x}$ sample need to be extended to include measurements of the oxygen partial pressure dependence of the oxygen stoichiometry and electrical conductivity relaxation studies to determine the diffusion and the surface exchange coefficients. Isotope transients obtained on the LSCF membranes indicate that heterogeneities exists in the membrane and the distribution of contributions of fast and slow areas need to be calculated and applied to improve the interpretation of the previous data. Isotopic transients need to be measured in LSCrF membrane at steady state, and the values of surface and bulk transport parameters obtained in the same manner as for LSCF.

References:

1. D. A. Berry, W. A. Surdoval and M. C. Williams, 222nd ACS National Meeting, Chicago, IL, United States, (2001).

2. S. P. Simner, J. F. Bonnett, N. L. Canfield, K. D. Meinhardt, V. L. Sprenkle, and J. W. Stevenson, *Electrochem. Solid State Lett.*, **5**, A173 (2002).

3. B. C. H. Steele, *J. Mater. Sci.*, **36**, 1053 (2001).

4. H. U. Anderson, X.-D. Zhou and F. Dogan, *Proceeding of the Electrochem. Soc. 2002*, (in press)

5. J. B. Yang, W. B. Yelon, W. J. James, Z. Chu, M. Kornecki, Y. X. Xie, X. D. Zhou, H. U. Anderson, A. G. Joshi and S. K. Malik, *Phys. Rev. B,* **66**, 184415 (2002).

6. D. E. Cox, *IEEE Trans. Magn.*, **MAG – 8**, 161 (1972).

7. S. E. Dann, D. B. Currie, M. T. Weller, M. F. Thomas, and A. D. Al-Rawwas, *J. Solid State Chem.,* **109**, 134 (1994).

BIBLIOGRAPHY:

N/A

LISTS OF ACRONYMS AND ABBREVIATIONS:

N/A